

Received June 29, 2020, accepted July 8, 2020, date of publication July 13, 2020, date of current version July 23, 2020.

Digital Object Identifier 10.1109/ACCESS.2020.3008727

3-D Printed Antenna Subsystem With Dual-Polarization and Its Test in System Level for Radiometer Applications

LI WU¹, HUI CHU^{1,2}, DI CAO³, SHUSHENG PENG¹, AND YONGXIN GUO^{4,5}, (Fellow, IEEE)

¹School of Electronic and Optical Engineering, Nanjing University of Science and Technology, Nanjing 210094, China

²School of Electronics and Information, Nantong University, Nantong 226019, China

³Nanjing Electronic Devices Institute, Nanjing 210023, China

⁴Department of Electrical and Computer Engineering, National University of Singapore, Singapore 117576

⁵National University of Singapore Suzhou Research Institute, Suzhou 215123, China

Corresponding author: Hui Chu (chuhui45@163.com)

This work was supported in part by the National Natural Science Foundation of China under Grant 61501234, in part by the Singapore National Research Foundation National Additive Manufacturing Innovation Cluster under Grant 2016231, and in part by the Natural Science Foundation of Jiangsu Province, China, under Grant BK20191184 and Grant BK20191288.

ABSTRACT A 3-D printed antenna subsystem, which proves its effectiveness in cost- & weight-reduction and reliability improvement over conventional CNC fabrication, is proposed in this paper. The proposed structure which integrates an orthogonal-mode transducer (OMT) and a corrugated horn is fully compatible to fabrication using high temperature resistant resin Acrylonitrile Butadiene Styrene (ABS) with 3-D printing technology, as well as coating using copper with electroless metallization method. Detailed design procedures are provided and a prototype operating at X-band is designed, fabricated and measured. Over the whole operating frequency range of 11.7 GHz~12.7 GHz, measured reflection coefficients are better than -22 dB and -12 dB for different polarization directions. A very good isolation better than 60 dB is achieved between two input ports. The cross polarization level is at least 30 dB lower than the co-polarization. Moreover, the effectiveness of the fabricated antenna is also verified in a polarimetric radiometer system.

INDEX TERMS Three-dimensional (3-D) printing, dual-polarization, orthogonal-mode transducer (OMT), horn antenna, radiometer.

I. INTRODUCTION

The polarimetric radiometer is able to provide more information compared to the single-polarized ones. Thus there is an increasing interest in applying the polarimetric radiometers in a variety of fields such as public security [1]–[4], remote sensing [5]–[7], etc. In remote sensing, the spaceborne polarimetric radiometers have been successfully used for measurements of wind speed and direction over sea surfaces, which is critical data for short-term weather forecasts, nowcasting, climatology and oceanography studies [5]. Also the polarimetric observations can be used to retrieve global soil moisture, vegetation water content, and land surface temperature simultaneously [6], [7]. The polarization information can be used to classify materials and to retrieve object

surface orientation, and it is also very helpful for object discrimination and identification [8]–[11].

An antenna subsystem which consists of an antenna and an orthogonal-mode transducer (OMT) is an essential subsystem for the polarimetric microwave radiometer system. In such a system, the isolation should always be large enough between two orthogonal polarizations, which is critical to achieve low cross-polarization levels [12]–[14]. Conventionally, the antenna and the OMT are fabricated separately and then interconnected with the waveguide flange. This method is convenient for fabrication but results in an uncertainty factor to the reliability of the whole system. This uncertainty factor will bring in latent danger and is unacceptable for those systems (e.g. spaceborne instrument) requiring extremely high reliability.

Compared to the individual fabrication, an integrated fabrication of antenna and OMT certainly can increase the reliability and reduce the weight, which are preferred for

The associate editor coordinating the review of this manuscript and approving it for publication was Giorgio Montisci.

spaceborne applications. However, it is usually difficult to achieve an integrated fabrication using conventional computerized numerical control (CNC) technology, due to its complex structure and small size.

Fortunately, it is capable to achieve such kind of integrated fabrication with the rapid development of 3-D printing technology. The 3-D printing technology, which is also known as additive manufacturing, is characterized by integration fabrication [15], weight reduction [16], cost effectiveness, eco-friendliness and process simplicity [17]–[20]. It has already been demonstrated in the fabrication of some microwave components with small size or complicated structure [21].

In this paper, an antenna subsystem consists of a corrugated horn and an OMT is designed and fabricated using a 3-D plastic printing technology. Simulated and experimental results are provided and discussed. For validation, a system level test is also conducted in a dual-polarization radiometer, by observing fresh water, lawn and concrete road. The fabricated prototype is competitive in both fabrication cost and time.

II. ANTENNA SUBSYSTEM DESIGN

The geometry of the antenna subsystem is presented in Fig. 1. This design is originated from in the Class I OMTs defined by Bøifot in [22], and the axially corrugated conical horn antenna in [23]. The presented antenna subsystem is mainly composed of three parts. Part I is the radiation section of the corrugated horn. Part II is the transition section with a length of L_1 from a circular waveguide input to a square waveguide. Part III is the OMT. It can be seen from Fig. 1 that there are 3 slots in the corrugated horn. The preferred value for the depth h of slots is $0.25-0.5\lambda_0$ (λ_0 is the wavelength of center frequency) [24]. The distance between adjacent slots is d and the width of slots is m . r_2 is radius of the input circular waveguide for the corrugated horn, which can ensure the propagation at its fundamental mode. r_1 is radius of the horn aperture, which is calculated using the below equation (1)

$$r_1 = L \tan \theta + a, \quad L = \frac{L_0 \tan \theta + 3(m + d)}{\tan \theta}, \quad (1)$$

For the OMT, the common port which uses a square waveguide is connected to the direct port and the coupled port with a tapered waveguide section. Lengths of the square waveguide section and the tapered waveguide section are L_2 and L_3 , respectively. A mode-matching technique is utilized in the tapered waveguide to reduce transmission loss for each port [25]. The signals are coupled to the coupling port through a coupling aperture.

A prototype of the antenna subsystem operating between 11.7 GHz and 12.7 GHz is designed. Dimensions of direct port and coupled port are both set to be 19.05 mm × 9.525 mm, according to a standard WR75 waveguide. To analyze effects of the coupling aperture on the S-parameters of the antenna subsystem, parametric studies of the coupling aperture are studied with ANSYS HFSS. Simulated

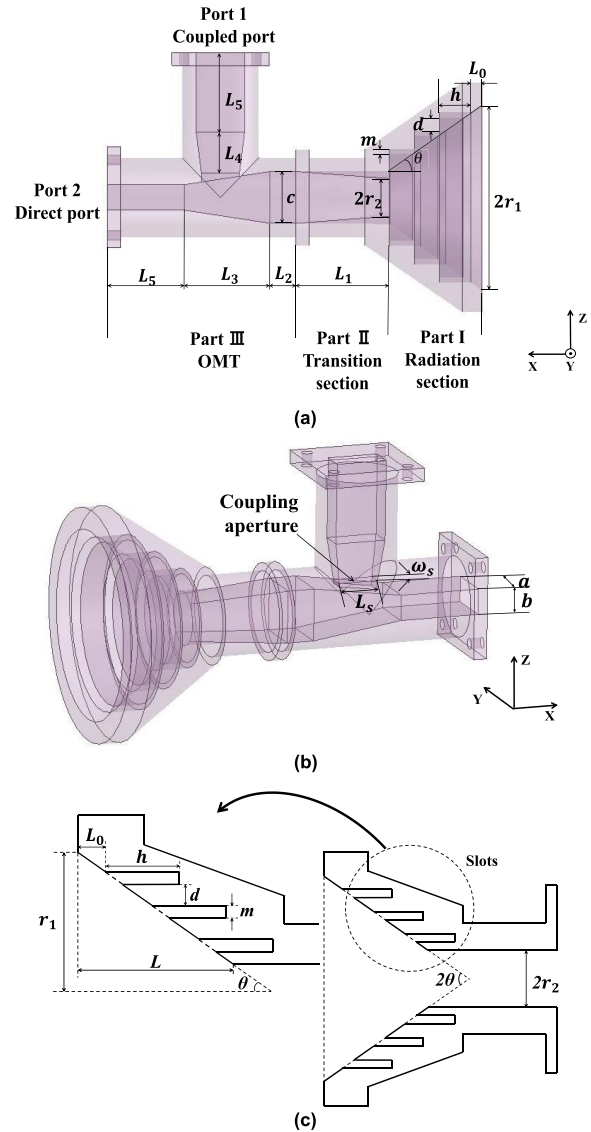


FIGURE 1. Geometry of the designed antenna subsystem. (a) Side view, (b) Perspective view and (c) Sketch of radiation section.

S-parameters are given in Fig. 2 with different dimensional parameters of the coupling aperture.

It can be observed from the above results that, the simulated $|S_{21}|$ and $|S_{11}|$ are better than -56 dB and -21 dB, respectively, when the coupling aperture length L_s varies within the range of 13.1–14.1 mm and the coupling aperture width W_s is within the range of 5.39–6.39 mm. The varying of coupling aperture length L_s will result in larger $|S_{11}|$ fluctuations in the lower frequency band, while the coupling aperture width W_s has more effects on $|S_{11}|$ in the higher frequency band. To reach an isolation level of -40 dB and an impedance matching of -10 dB during the designed working frequency band, dimensions of the presented antenna subsystem are well optimized. Detailed dimensions are summarized in Table 1.

In our design, the size of the waveguide connected with direct port and coupled port are designed to make sure that only the dominant TE_{10} -mode is propagated. According to

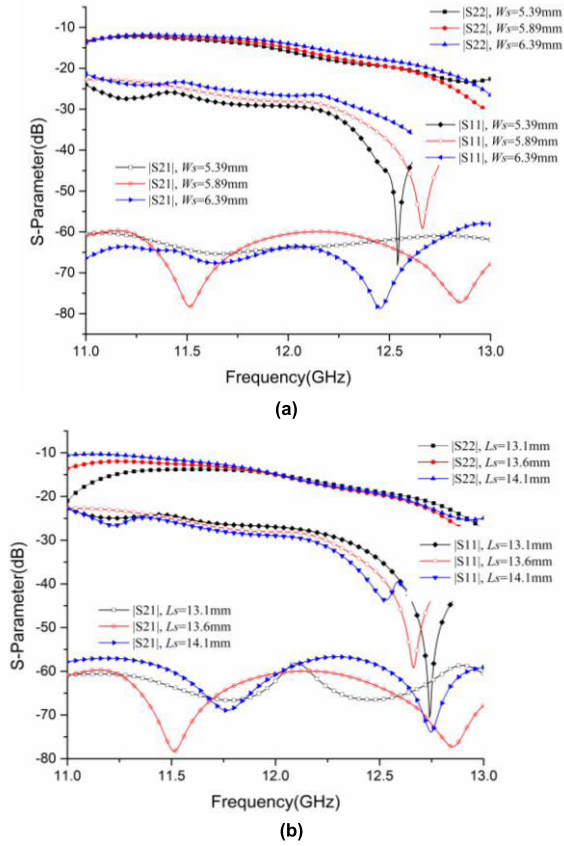


FIGURE 2. Simulated S-parameters with different coupling aperture dimensions: (a) $W_s = 5.39, 5.89$ and 6.39 mm, $L_s = 13.6$ mm and (b) $W_s = 5.89$ mm, $L_s = 13.1, 13.6$ and 14.1 mm.

the coordinate system illustrated in Fig. 1, the field distribution of TE_{10}^x propagated in the direct-arm and TE_{10}^z propagated in coupled-arm can be written as (2) and (3), respectively. It can be seen that, the propagated modes in different arms are orthogonal to each other and therefore leads to orthogonal E-field directions in the far-field, satisfying the definition of the dual-polarization.

$$\begin{cases} E_z = \frac{-jw\mu a}{\pi} A_{10} \sin \frac{\pi y}{a} e^{j\beta x} \\ H_y = \frac{j\beta a}{\pi} A_{10} \sin \frac{\pi y}{a} e^{j\beta x} \\ H_x = A_{10} \cos \frac{\pi y}{a} e^{j\beta x} \\ E_y = E_x = H_z = 0 \end{cases} \quad (2)$$

$$\begin{cases} E_y = \frac{-jw\mu a}{\pi} A_{10} \sin \frac{\pi x}{a} e^{j\beta z} \\ H_x = \frac{j\beta a}{\pi} A_{10} \sin \frac{\pi x}{a} e^{j\beta z} \\ H_z = A_{10} \cos \frac{\pi x}{a} e^{j\beta z} \\ E_x = E_z = H_y = 0 \end{cases} \quad (3)$$

Field distributions at the interface between the circular waveguide and horn aperture are also plotted for a validation of the dual-polarization. Simulated field distributions are plotted in Fig. 3. It is seen that, transmission mode of TE_{11}^V is excited by the direct port, while TE_{11}^H mode is excited by the

TABLE 1. Optimized dimensions of the designed antenna subsystem.

Symbol	Value	Symbol	Value
r_1	37.40 mm	L_0	4.60 mm
h	12.30 mm	L_1	37.00 mm
d	4.90 mm	L_2	10.18 mm
m	2.00 mm	L_3	33.87 mm
r_2	35.30 mm	L_4	15.54 mm
θ	35°	L_5	30.00 mm
L_s	13.60 mm	a	19.05 mm
W_s	5.89 mm	b	9.525 mm
		c	19.54 mm

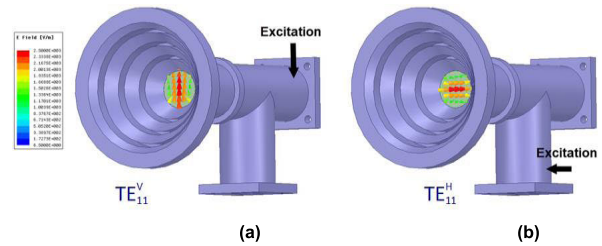


FIGURE 3. Simulated E-field distributions at the interface between the circular waveguide and horn aperture. (a) TE_{11}^V mode excited by the direct port and (b) TE_{11}^H mode excited by the coupled port.

coupled port. Since these two modes are orthogonal to each other, a dual-polarization of radiation from the corrugated horn in the farfield can be generated when different port is excited.

III. FABRICATION PROCESS

The fabricated antenna is shown in Fig. 4. The fabrication of the designed antenna subsystem involves two main steps: 1) dielectric component structure fabrication; and 2) metalization process. For the dielectric component structure, it is fabricated with the high temperature resistant resin Acrylonitrile Butadiene Styrene (ABS) using the fused deposition modeling (FDM) technology. The component is built layer by layer with a dual extruder 3-D printer and an inner support structure is added during the printing process. The employed support material is water-soluble polyvinyl alcohol (PVAL). Lastly the support structure is removed by dissolving the support material to finalize the antenna subsystem model

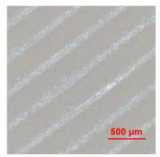



FIGURE 4. Photograph of the fabricated antenna subsystem.

printing. Subsequently, a standard commercial electroless metallization process is adopted in this paper to ensure that the interior surfaces of the horn and the OMT can be fully metallized. The surface of the 3-D printed structure is oiled with organic solvent firstly, and then it is roughened by using a mixture of sulfuric acid and chromic acid to form pits on the surface to increase the adhesion area of metal. A sensitizer is employed to deposit a liquid film on the surface, and silver nitrate and nickel sulfate are added to form a thin metallic layer on the dielectric structure. Next, the structure is processed with electroless copper plating. Finally, the component is plated with a thick layer of copper to form a metal surface with a certain thickness.

In order to understand better with the printing quality of the 3-D Printing process, the antenna subsystem is taken into a microscopic inspection using Nikon ECLIPSE L200N and the surface roughness is listed in Table 2. As observed from Table 2, the surface roughness before and after the metallization is $5.89 \mu\text{m}$ and $4.45 \mu\text{m}$, respectively, which means the adhering copper foil will improve the surface roughness.

TABLE 2. Microscopic inspection on material surface.

3DP Method	FDM	
	Adhered Copper Foil?	Yes
Adhered Copper Foil?	No	Yes
Surface (scale: 500 μm)		
Ra (μm)	5.89	4.45

IV. MEASUREMENT AND PERFORMANCE COMPARISON

A. S-PARAMETERS

The S-parameters of the designed antenna subsystem are measured by a Keysight Network Analyzer N5244A. Measured and simulated S-parameter results are presented in Fig. 5, where good agreement between measured and simulated results can be seen. The measured $|S_{11}|$ and $|S_{22}|$ are lower than -22dB and -12dB during the operating frequency band from 11.7 to 12.7 GHz, respectively. For $|S_{21}|$ which indicates the coupling between the direct port and the coupled port, a high isolation lower than -60dB is achieved across the working frequency band.

B. RADIATION PATTERN

The radiation patterns of the fabricated antenna subsystem are measured in the anechoic chamber of Nanjing University of Science and Technology. The measured and simulated radiation patterns for direct port and coupled port at frequencies of 11.7 GHz, 12.2 GHz and 12.7 GHz are shown in Figs. 6-7, respectively, which are all in satisfactory agreement.

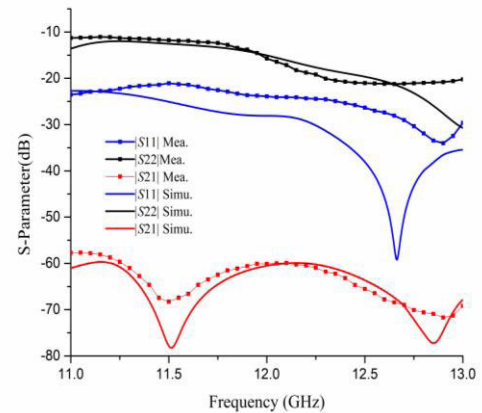


FIGURE 5. Measured and simulated S-parameters of the designed antenna subsystem. (Port 1: coupled port, Port 2: direct port).

It can be seen that the cross polarization during the main lobe is below -29dB over the operating frequency band. When feeding from the direct port, there is a minor discrepancy between simulation and measurement. The cross polarization remains lower than -26dB across the operating band. The maximum discrepancy in the radiation patterns of $\varphi = 0^\circ$ and $\varphi = 90^\circ$ at $\pm 40^\circ$ (angles subtended at the feed point by the upper and lower edges of the reflector) is 4 dB at 11.7 GHz, 12.2 GHz and 12.7 GHz for the above measurement results. In view of that the maximum edge taper is -13dB among different frequencies for the direct port or the coupled port excitation, the edge taper error will not result in a great difference for performances of the whole radiometer reflector antenna.

It is also seen in Fig. 6 and 7 that, the front-to-back ratio is larger than 22 dB for the direct port at the center working frequency of 12.2 GHz in the measurement, while it is larger than 26 dB for the coupled port. Similar performance can also be achieved at 11.7 GHz and 12.7 GHz, respectively.

A good symmetry between E- & H-planes can be observed in radiation patterns. In the measurement, similar 3-dB beamwidths are achieved between E- & H-plane patterns at 11.7 GHz, 12.2 GHz and 12.7 GHz. The beam-widths gradually differ to each other until the gain is smaller than its peak than 5 dB.

A performance comparison is conducted with respect to other types of antennas from aspects of impedance bandwidth, achievable gain, profile, polarization purity, front-to-back ratio and symmetry between E-&H-plane patterns. It is seen in Table 3 that, within mentioned types of antennas, the magneto-electric dipole and corrugated horn antenna are the only two that can simultaneously achieve required polarization purity, front-to-back ratio and symmetry between E-&H-plane patterns for the radiometer application. However, the achievable gain of the corrugated horn antenna is much larger than the magneto-electric dipole, which makes it more suitable for radiometer applications.

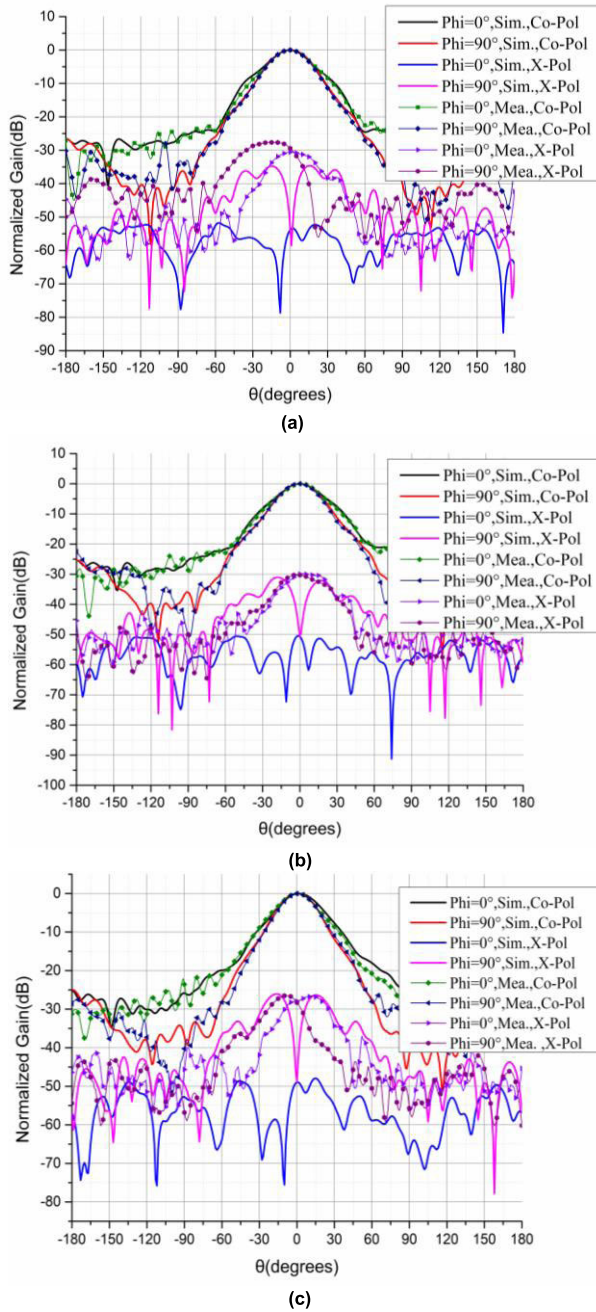


FIGURE 6. Measured and simulated radiation patterns at (a) 11.7 GHz, (b) 12.2 GHz and (c) 12.7 GHz when feeding from direct port.

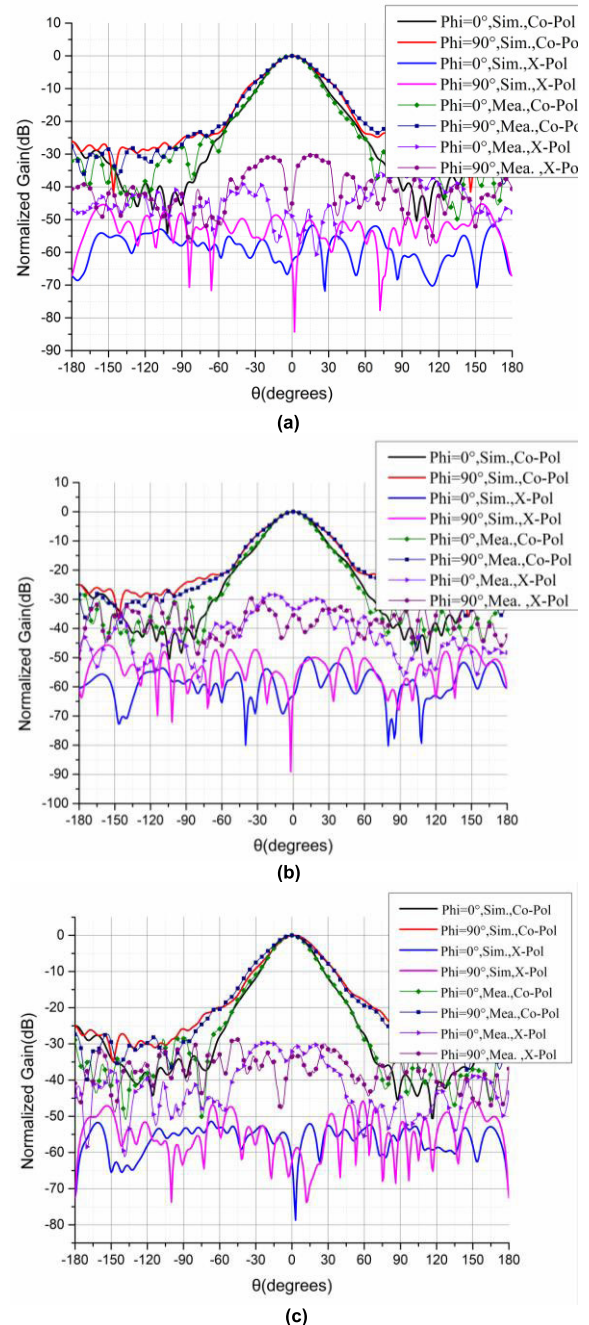


FIGURE 7. Measured and simulated radiation patterns at (a) 11.7 GHz, (b) 12.2 GHz and (c) 12.7 GHz when feeding from coupled port.

C. LOSS DYNAMICS

A study of loss dynamics is conducted at 12.2 GHz for the direct port (port 2). The overall loss of the fabricated antenna/OMT subsystem is calculated by comparing the measured gain and simulated directivity. The measured gain [as in Fig. 8] and simulated directivity is 15.12 dBi and 15.6 dBi, respectively. In this case, the overall loss is found to be 0.48 dB, which includes return loss, insertion loss of the SMA-to-waveguide transition, surface roughness loss and metallic loss of plated copper. Details of the losses are as below:

- Return loss: The measured return loss is -17.5 dB, which corresponds to a loss of 0.008 dB when it is converted to the transmission case.
- Insertion loss of the SMA-to-waveguide transition: The insertion loss can be measured by using two transitions arranged in a back-to-back configuration. Measured insertion loss is 0.68 dB for this configuration, which means 0.34 dB insertion loss for each individual transition.
- Surface roughness loss and metallic loss: Values of these two kinds of loss are hard to be measured. As an alternative,

TABLE 3. Performance comparison between different kinds of antenna elements.

	Fractional Impedance Bandwidth	Gain at f_0	Profile	Polarization Purity	Front-to-Back Ratio	Symmetry of 3-dB Beamwidth between E- & H-Plane Patterns
Patch [26]	14.1% (3.3~3.8 GHz)	≈ 9.3 dBi	$\approx 0.12 \lambda_0$	>20 dB	<10 dB	45° VS 46°
Metallic Waveguide Slot [27]	9.4% (16.2~17.8 GHz)	≈ 22 dBi	$\approx 1.2 \lambda_0$	>32 dB	>20 dB	10° VS 20°
Rectangle DRA [28]	7% (3.6~3.86 GHz)	≈ 6 dBi	$\approx 0.2 \lambda_0$	>25 dB	<10 dB	61° VS 64°
Magneto-Electric Dipole [29]	65.9% (1.72~3.4 GHz)	≈ 9 dBi	$\approx 0.23 \lambda_0$	>20 dB	>18 dB	58.8° VS 58.8°
Corrugated Horn	16.7% (11~13 GHz)	≈ 15 dBi	$\approx 6.5 \lambda_0$	>27.5 dB	>25 dB	28.9° VS 28.1°

TABLE 4. Performance comparison between antenna/OMT subsystem fabricated by CNC and 3-D printing.

	Return Loss	Radiation Gain	Fabrication Time	Fabrication Cost	Weight	Integrative Fabrication
Conventional Fabrication	<-10 dB for 11~13 GHz	>14.9 dBi for 11~13 GHz	≈ 6 hours	≈ 3000 RMB	392g	No
3-D Printing Fabrication	<-10 dB for 11~13 GHz	>14.9 dBi for 11~13 GHz	≈ 8 hours	≈ 600 RMB	74g	Yes

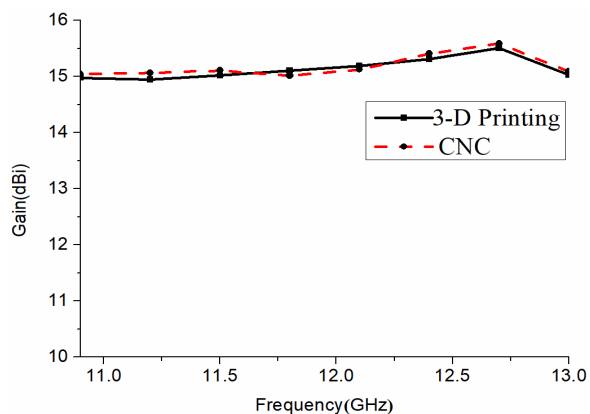


FIGURE 8. Measured gain of prototypes fabricated by CNC and 3-D printing technology.

the sum of them is evaluated by subtracting the return loss and insertion loss of transition from the overall loss, which approximately equals to 0.132 dB (≈ 0.48 dB - 0.008 dB - 0.34 dB).

D. PERFORMANCE COMPARISON

A same antenna/OMT subsystem [as in Fig. 9] is fabricated using the CNC technology for a performance assessment versus 3-D printing, from aspects of their return loss, radiation gain, fabrication time, fabrication cost, weight and reliability. Results are summarized in Table 4.

Measured results of return loss and gain are compared in Fig. 10 and 8, respectively. It is seen that, similar electric

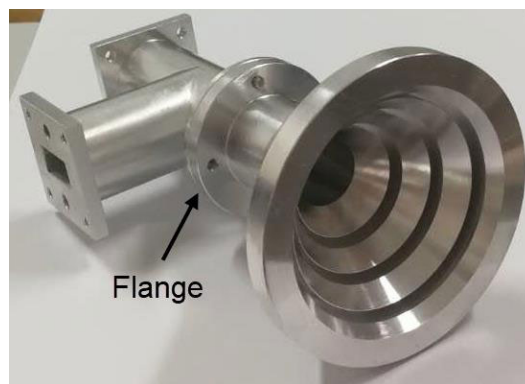


FIGURE 9. Antenna/OMT subsystem Fabricated using CNC milling.

performance is achieved between them. The maximum gain difference is less than 0.1 dB. Meanwhile, as mentioned in Table 3, their fabrication time is also comparable to each other. However, the fabrication cost including dielectric component printing and post-process metallization is only around 1/5 of the CNC fabrication using metal blocks. Moreover, the overall weight is reduced by 4/5 when using the 3-D printing fabrication, which is critical important for spaceborne applications. It also needs to be addressed that, in the CNC fabrication, the part of OMT [as illustrated in Fig. 1(a)] needs to be separately fabricated with respect to other parts, and then connected together using a flange [as illustrated in Fig. 9]. This kind of a fabrication reduces the reliability of the whole antenna/OMT subsystem.

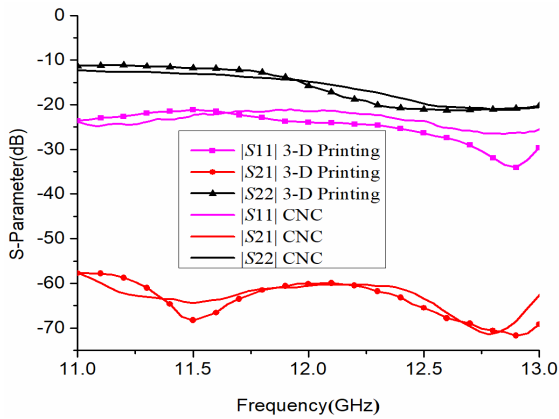


FIGURE 10. Comparison of measured return loss between antenna/OMT subsystem fabricated by CNC and 3-D printing technology.

V. SYSTEM-LEVEL TEST

The designed antenna subsystem is also applied in a dual-polarization radiometer for natural object observations to demonstrate its performances. As illustrated in Fig. 7, the dual-polarization radiometer consists of a parabolic reflector, an antenna subsystem which consists of a corrugated horn and an OMT, and a two-channel superheterodyne receiver with local oscillators operating at 10.7 GHz. Each receiver channel consists of a noise source, a coupler, a low noise block (LNB) for SAT-TV applications, an intermediate frequency amplifier unit and a video amplifier (VA). The LNB working as the core of the receiver is an off-the-shelf device for the commercial SAT-TV receiver, which features a high performance and a low cost [30]. Two orthogonal linear polarized components are separated by the OMT, amplified and then down converted to 1000 MHz ~ 2000 MHz in the intermediate frequency (IF) section. Then, the amplified IF signal is fed into the square-law detector and the video amplifier. Finally, the output signal of the video amplifier is acquired and processed to derive the observed brightness temperature.

The LNBS are characterized by a noise figure of 0.8 dB, a conversion gain of 55 dB and an input voltage standing wave ratio (VSWR) of 2.2 [31]. The local oscillator features

phase noise of -85 dBc/Hz at 10 kHz offset from the carrier frequency of 10.7 GHz. The input radio frequency signal between 11.7 GHz ~ 12.7 GHz is down converted to the IF signal in the frequency range of 1 GHz ~ 2 GHz. The image frequencies between 8.7 GHz ~ 9.7 GHz are rejected by more than 40 dB by a bandpass filter integrated in the LNB.

The observed objects are fresh water, lawn and concrete road. The dual-polarization radiometer is calibrated before observation and its output brightness temperature correlates the object reflectivity with

$$T_h = T_{in} \cdot r_h + T_0 \cdot (1 - r_h), \tag{4}$$

$$T_v = T_{in} \cdot r_v + T_0 \cdot (1 - r_v), \tag{5}$$

where T_h and T_v are the horizontal and vertical polarization brightness temperature, respectively. T_{in} is the incidence radiometric temperature on the object. T_0 is the brightness temperature of object. r_h and r_v are the horizontally and vertically polarized reflectivities, respectively.

In the experiment, the temperatures of the environment, the concrete road and the lawn are 16.5 °C, 17.8 °C and 16.7 °C, respectively. The experimental results are recorded under different incidence angles of 30°, 45° and 60°. When the incidence wave is from air into the observed medium, it is known from the Fresnel equation that the reflectivity for horizontally and vertically polarized incidence can be separately expressed as

$$r_h = \left| \frac{\cos \theta_i - n_2 \sqrt{1 - (\frac{1}{n_2} \sin \theta_i)^2}}{\cos \theta_i + n_2 \sqrt{1 - (\frac{1}{n_2} \sin \theta_i)^2}} \right|^2, \tag{6}$$

$$r_v = \left| \frac{\sqrt{1 - (\frac{1}{n_2} \sin \theta_i)^2} - n_2 \cos \theta_i}{\sqrt{1 - (\frac{1}{n_2} \sin \theta_i)^2} + n_2 \cos \theta_i} \right|^2, \tag{7}$$

where θ_i is the incidence angle, $n_2 = \sqrt{\epsilon}$ is the refractive index of the observed medium, and ϵ is the permittivity. The horizontally and vertically polarized reflectivities under different incidence angles can be derived with a given permittivity. The permittivity of fresh water can be calculated

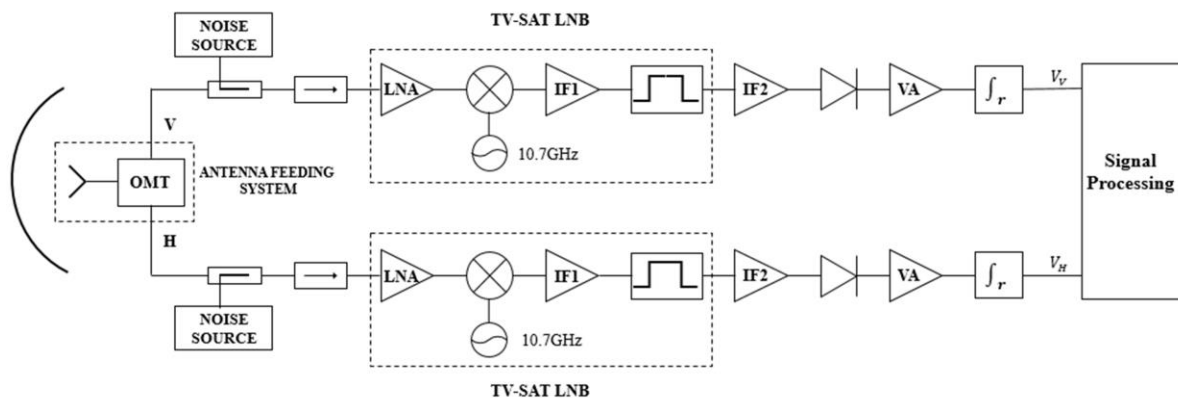


FIGURE 11. Block diagram of the dual-polarization radiometer.

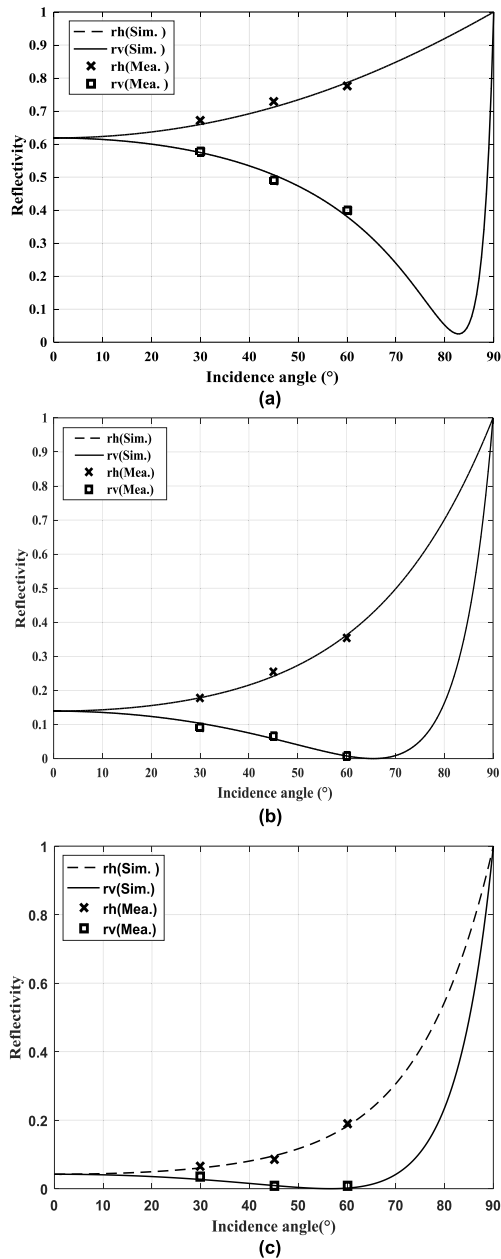


FIGURE 12. Experimental and theoretical polarized reflectivity for different objects. (a) Fresh water, (b) concrete road and (c) lawn.

with the Liebe's model which offers good results through the frequency range of 1~1000 GHz [32]:

$$\left\{ \begin{array}{l} \varepsilon(T_K, f) = \frac{\varepsilon_0 - \varepsilon_1}{1 - i(f/\gamma_1)} + \frac{\varepsilon_1 - \varepsilon_2}{1 - i(f/\gamma_2)} + \varepsilon_2 \\ \varepsilon_1 = 0.0671\varepsilon_0 \\ \theta = 1 - \frac{300}{T_K} \\ \varepsilon_2 = 3.52 + 7.52\theta \\ \gamma_1 = 20.20 + 146.4\theta + 316\theta^2 \\ \varepsilon_0 = 77.66 - 103.3\theta \\ \gamma_2 = 39.8\gamma_1 \end{array} \right. \quad (8)$$

The calculated horizontal and vertical reflectivities in theory are shown in Fig. 12. Theoretical data are calculated with the permittivity of 4.8 for the concrete road and 2.3 for the lawn. Also the measured horizontal and vertical reflectivity results for the concrete road and the lawn are presented respectively.

It can be seen from the figures that the experimental results agree well with the theoretical data. The error between experiment and prediction is smaller than 0.02. The measurement results demonstrate the satisfactory performances of the designed dual-polarization radiometer and the fabricated antenna subsystem.

VI. CONCLUSION

An antenna subsystem which consists of an OMT and a corrugated horn is designed, fabricated and measured with the 3-D printing plastic technology for polarimetric radiometer system in this paper. The presented integrated design and fabrication approach can reduce the weight and increase the reliability of the antenna subsystem. The measured S-parameters and radiation patterns are given and compared with simulated ones. In addition, the fabricated antenna subsystem is integrated into a dual-polarization radiometer system for natural objects observation to evaluate its performances. The measured horizontally and vertically polarized reflectivity results agree well with predicted values. The fabricated antenna subsystem demonstrates a great potential of 3-D printing technology for microwave components prototyping which is competitive in fabrication cost, weight and reliability.

REFERENCES

- [1] J. P. Wilson, C. A. Schuetz, C. E. Harrity, S. Kozacik, D. L. K. Eng, and D. W. Prather, "Measured comparison of contrast and crossover periods for passive millimeter-wave polarimetric imagery," *Opt. Express*, vol. 21, no. 10, pp. 12899–12907, 2013.
- [2] E. Gonzalez-Sosa, R. Vera-Rodriguez, J. Fierrez, and V. M. Patel, "Exploring body shape from mmW images for person recognition," *IEEE Trans. Inf. Forensics Security*, vol. 12, no. 9, pp. 2078–2089, Sep. 2017.
- [3] S. Liao, N. Gopalsami, T. W. Elmer, E. R. Koehl, A. Heifetz, K. Avers, E. Dieckman, and A. C. Raptis, "Passive millimeter-wave dual-polarization imagers," *IEEE Trans. Instrum. Meas.*, vol. 61, no. 7, pp. 2042–2050, Jul. 2012.
- [4] L. Wu, J. Q. Zhu, S. S. Peng, Z. L. Xiao, and Y. K. Wang, "Post-processing Techniques for Polarimetric Passive Millimeter Wave Imagery," *Appl. Comput. Electrom.*, vol. 33, no. 5, pp. 512–518, May 2018.
- [5] P. W. Gaiser, K. M. St Germain, E. M. Twarog, G. A. Poe, W. Purdy, D. Richardson, W. Grossman, W. L. Jones, D. Spencer, G. Golba, J. Cleveland, L. Choy, R. M. Bevilacqua, and P. S. Chang, "The WindSat spaceborne polarimetric microwave radiometer: Sensor description and early orbit performance," *IEEE Trans. Geosci. Remote Sens.*, vol. 42, no. 11, pp. 2347–2361, Nov. 2004.
- [6] L. Li, P. W. Gaiser, B.-C. Gao, R. M. Bevilacqua, T. J. Jackson, E. G. Njoku, C. Rudiger, J.-C. Calvet, and R. Bindlish, "WindSat global soil moisture retrieval and validation," *IEEE Trans. Geosci. Remote Sens.*, vol. 48, no. 5, pp. 2224–2241, May 2010.
- [7] R. M. Parinussa, T. R. H. Holmes, and R. A. M. de Jeu, "Soil moisture retrievals from the WindSat spaceborne polarimetric microwave radiometer," *IEEE Trans. Geosci. Remote Sens.*, vol. 50, no. 7, pp. 2683–2694, Jul. 2012.
- [8] Y. Cheng, F. Hu, L. Gui, L. Wu, and L. Lang, "Polarization-based method for object surface orientation information in passive millimeter-wave imaging," *IEEE Photon. J.*, vol. 8, no. 1, pp. 1–12, Feb. 2016.

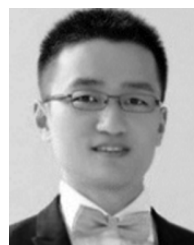
- [9] F. Hu, Y. Cheng, L. Gui, L. Wu, X. Zhang, X. Peng, and J. Su, "Polarization-based material classification technique using passive millimeter-wave polarimetric imagery," *Appl. Opt.*, vol. 55, pp. 8690–8697, Nov. 2016.
- [10] X. Lu, Z. Xiao, and J. Xu, "Linear polarization characteristics for Terrain identification at millimeter wave band," *Chin. Opt. Lett.*, vol. 12, Oct. 2014, Art. no. 101201.
- [11] S. Yeom, D. Lee, H. Lee, J. Son, and V. P. Gushin, "Vector clustering of passive millimeter wave images with linear polarization for concealed object detection," *Prog. Electromagn. Res. Lett.*, vol. 39, pp. 169–180, 2013.
- [12] A. Duric, A. Magun, A. Murk, C. Matzler, and N. Kampfer, "The fully polarimetric imaging radiometer SPIRA at 91 GHz," *IEEE Trans. Geosci. Remote Sens.*, vol. 46, no. 8, pp. 2323–2336, Aug. 2008.
- [13] W. Hongjian, H. Qiyang, Y. Min, Z. Dehai, D. Xingchao, L. Yang, and C. Xue, "Multi-frequency dual polarisation radiometer common aperture antenna feeding system," *IET Microw., Antennas Propag.*, vol. 12, no. 11, pp. 1765–1770, Jul. 2018.
- [14] H. Saeidi-Manesh and G. Zhang, "High-isolation, low cross-polarization, dual-polarization, hybrid feed microstrip patch array antenna for MPAR application," *IEEE Trans. Antennas Propag.*, vol. 66, no. 5, pp. 2326–2332, May 2018.
- [15] M. A. Al-Tarifi and D. S. Filipovic, "On the design and fabrication of W-band stabilised-pattern dual-polarised horn antennas with DMLS and CNC," *IET Microw., Antennas Propag.*, vol. 11, no. 14, pp. 1930–1935, Nov. 2017.
- [16] M. Ferrando-Rocher, J. I. Herranz-Herruzo, A. Valero-Nogueira, and B. Bernardo-Clemente, "Performance assessment of gap-waveguide array antennas: CNC milling versus three-dimensional printing," *IEEE Antennas Wireless Propag. Lett.*, vol. 17, no. 11, pp. 2056–2060, Nov. 2018.
- [17] F. Calignano, D. Manfredi, E. Paola Ambrosio, S. Biamino, M. Lombardi, E. Atzeni, A. Salmi, P. Minetola, L. Iuliano, and P. Fino, "Overview on additive manufacturing technologies," *Proc. IEEE*, vol. 105, no. 4, pp. 593–612, Apr. 2017.
- [18] J.-C.-S. Chieh, B. Dick, S. Loui, and J. D. Rockway, "Development of a ku-band corrugated conical horn using 3-D print technology," *IEEE Antennas Wireless Propag. Lett.*, vol. 13, pp. 201–204, 2014.
- [19] C. Guo, X. Shang, M. J. Lancaster, and J. Xu, "A 3-D printed lightweight X-Band waveguide filter based on spherical resonators," *IEEE Microw. Wireless Compon. Lett.*, vol. 25, no. 7, pp. 442–444, Jul. 2015.
- [20] B. Zhang, Y.-X. Guo, H. Zirath, and Y. P. Zhang, "Investigation on 3-D-printing technologies for millimeter-wave and terahertz applications," *Proc. IEEE*, vol. 105, no. 4, pp. 723–736, Apr. 2017.
- [21] W. J. Otter and S. Lucyszyn, "Hybrid 3-D-Printing technology for tunable THz applications," *Proc. IEEE*, vol. 105, no. 4, pp. 756–767, Apr. 2017.
- [22] A. M. Bøifot, "Classification of ortho-mode transducers," *Eur. Trans. Telecommun.*, vol. 2, no. 5, pp. 503–510, Sep. 1991.
- [23] A. C. Balanis, "Aperture antennas: Waveguides and horns," in *Modern Antenna Handbook*. Hoboken, NJ, USA: Wiley, 2008, pp. 97–156.
- [24] C. Lin, H. Chen, and W. Wu, *Modern Antenna Design*. Beijing, China: China Post and Telecom Press, 1990.
- [25] P. K. Verma and R. Kumar, "Realization of ku-band ortho mode transducer with high port to port isolation," *Prog. Electromagn. Res. Lett.*, vol. 74, pp. 111–115, 2018.
- [26] J. Lu, Z. Kuai, X. Zhu, and N. Zhang, "A high-isolation dual-polarization microstrip patch antenna with Quasi-Cross-Shaped coupling slot," *IEEE Trans. Antennas Propag.*, vol. 59, no. 7, pp. 2713–2717, Jul. 2011.
- [27] H. Luo, Y. Xiao, X. Lu, and H. Sun, "Design of a dual-polarization single-ridged waveguide slot array with enhanced bandwidth," *IEEE Antennas Wireless Propag. Lett.*, vol. 18, no. 1, pp. 138–142, Jan. 2019.
- [28] Y. Gao, Z. Feng, and L. Zhang, "Compact CPW-fed dielectric resonator antenna with dual polarization," *IEEE Antennas Wireless Propag. Lett.*, vol. 10, pp. 544–547, 2011.
- [29] B. Qun Wu and K.-M. Luk, "A broadband dual-polarized magneto-electric dipole antenna with simple feeds," *IEEE Antennas Wireless Propag. Lett.*, vol. 8, pp. 60–63, 2009.
- [30] F. Alimenti, S. Bonafoni, S. Leone, G. Tasselli, P. Basili, L. Roselli, and K. Solbach, "A low-cost microwave radiometer for the detection of fire in forest environments," *IEEE Trans. Geosci. Remote Sens.*, vol. 46, no. 9, pp. 2632–2643, Sep. 2008.
- [31] Swedish Microwave, AB Motala, Sweden. (2004). *SMW LNB DRO-Low Phase Noise Single Band DRO LNB*. [Online]. Available: <http://www.smw.se>

- [32] C. Mätzler, Ed., *Thermal Microwave Radiation: Applications for Remote Sensing*. Edison, NJ, USA: IET, 2006.



passive microwave imaging, and millimeter wave systems.

LI WU received the B.S., M.S., and Ph.D. degrees in electronic engineering from the Nanjing University of Science and Technology, Nanjing, China, in 2003, 2005, and 2009, respectively. Since 2009, he has been a Lecturer with the School of Electronic and Optical Engineering, Nanjing University of Science and Technology. He has authored or coauthored more than 30 journals or conference papers. He holds five Chinese patents. His research interests include millimeter wave antennas,



He has authored or coauthored 30 international journals or conference papers. He holds two Chinese patents. His current research interests include millimeter-wave antennas, filters, and bio-medical antennas for endoscope applications.

HUI CHU was born in Nantong, China, in 1985. He received the B.S. degree in electric and information engineering and the Ph.D. degree from the Nanjing University of Science and Technology, Nanjing, China, in 2007 and 2012, respectively.

He was a Lecturer with Nantong University, Nantong, from January 2013 to March 2018. He joined the School of Electronic and Optical Engineering, Nanjing University of Science and Technology, in April 2018, as an Associate Professor.



DI CAO received the B.S. and M.S. degrees in electronic information and communication engineering from the Nanjing University of Science and Technology, Nanjing, China, in 2016 and 2019, respectively. His research interest includes microwave antennas for radar applications.



and coauthored two books and more than 70 articles. His current research interests include millimeter wave detection technology, microwave and millimeter wave radiation measurement, the application of embedded systems and intelligent sensing, and measurement technology.

SHUSHENG PENG received the B.S. degree from Xiamen University, in 1987, the M.S. degree from the Xi'an Institute of Space Radio Technology, in 1990, and the Ph.D. degree from the Purple Mountain Observatory, Chinese Academy of Sciences, in 1995.

Since 1997, he has been an Associate Professor and then a Professor with the School of Electronic and Optical Engineering, Nanjing University of Science and Technology.



YONGXIN GUO (Fellow, IEEE) received the B.Eng. and M.Eng. degrees in electronic engineering from the Nanjing University of Science and Technology, Nanjing, China, in 1992 and 1995, respectively, and the Ph.D. degree in electronic engineering from the City University of Hong Kong, in 2001.

He was with the Institute for Infocomm Research, Singapore, as a Research Scientist, from September 2001 to January 2009. He joined the Department of Electrical and Computer Engineering (ECE), National University of Singapore (NUS), in February 2009, as an Assistant Professor, and was promoted to a Professor with tenure, in January 2019. Concurrently, he is a Senior Investigator at the National University of Singapore Suzhou Research Institute (NUSRI), Suzhou, China, and the Director of the Center of Advanced Microelectronic Devices, NUSRI. He has authored or coauthored 154 international journal articles and 162 international conference papers. His publications have been cited by others more than 1189 times and the H-index is 22 (source: Scopus). He holds one granted Chinese patent, one granted U.S. patent, one filed PCT patent, three filed Chinese patents, and

one filed U.S. Provisional Patent. His current research interests include microstrip antennas for wireless communications, implantable/wearable antennas for biomedical applications, wireless power and RF energy harvesting, microwave circuits, and MMIC modeling and design. He has supervised seven Ph.D. students at NUS.

Dr. Guo was a recipient of the Young Investigator Award 2009 at the National University of Singapore, the 2013 “RajMitra” Travel Grant Senior Researcher Award and the Best Poster Award in 2014 International Conference on Wearable & Implantable Body Sensor Networks (BSN2014), Zürich, Switzerland. He was the General Chair of the IEEE MTT-S International Microwave Workshop Series 2013 on “RF and Wireless Technologies for biomedical and Healthcare Applications” (IMWS-Bio2013), Singapore. He served as the Technical Program Committee (TPC) Co-Chair for the IEEE International Symposium on Radio Frequency Integration Technology (RFIT2009). He has been a TPC member and the session chair for numerous conferences and workshops. He is serving as an Associate Editor of the IEEE ANTENNAS AND WIRELESS PROPAGATION LETTERS and *IET Microwaves, Antennas & Propagation*.

• • •